nanomaterials

MDPI

Article

Phase-Dependent Electrocatalytic Activity of Small-Sized Nickel Sulfide Hollow Nanocrystals for Efficient Alkaline Water Electrolysis

Chunmei Lv [1], Hailing Xu [2], Fei Chen [1], Jing Wang [1], Linhong Shi [1], Gege Wang [1], Yitong Wang [1] and Xiuwen Wang [1,*]

[1] College of Chemistry and Chemistry Engineering, Qiqihar University, Qiqihar 161006, China
[2] Qiqihar Environmental Monitoring Station, Qiqihar 161006, China
* Correspondence: xwwang@qqhru.edu.cn

Abstract

Phase engineering of nickel sulfides represents a promising route to develop low-cost bifunctional electrocatalysts toward alkaline water electrolysis, yet the explicit correlation between the crystalline phase and electrocatalytic performance remains insufficiently understood. Herein, small-sized nickel sulfide hollow nanocrystals with tailored crystal phases, including pure Ni_3S_2, a mixed Ni_xS_y phase (which consists of Ni_3S_2 and NiS), and pure NiS, are prepared via modulating the thioacetamide dosage in a Schlenk reaction system. Systematic electrochemical measurements demonstrate that Ni_3S_2 exhibits superior hydrogen evolution reaction (HER) and oxygen evolution reaction (OER) catalytic activity relative to the mixed-phase Ni_xS_y and pure NiS. When constructed as a $Ni_3S_2||Ni_3S_2$ electrolyzer for alkaline water electrolysis, a low cell voltage of 1.55 V is obtained at 10 mA cm^{-2}, which is much lower than that of the $Ni_xS_y||Ni_xS_y$ counterpart (1.66 V). Additionally, the Ni_3S_2-based electrolyzer exhibits exceptional durability, retaining nearly full activity after 100 h of continuous operation with merely a 0.40% performance decay. This work establishes a clear phase–activity relationship for nickel sulfide nanomaterials and offers a facile synthetic strategy for designing high-performance non-noble metal bifunctional electrocatalysts toward practical alkaline water electrolysis.

Keywords: sulfide; phase; bifunctional electrocatalyst; overall water splitting; stability

1. Introduction

Alkaline water electrolysis presents a promising sustainable route for green hydrogen (H_2) production, which consists of the cathodic hydrogen evolution reaction (HER) and anodic oxygen evolution reaction (OER) [1–4]. Alkaline HER follows the Volmer–Heyrovsky route, where water dissociation generates H* intermediate, followed by H_2 desorption. For OER, the adsorbate evolution mechanism (AEM) dominates, involving successive transformation of OH* → O* → OOH* intermediates before O_2 release. However, HER and OER suffer from sluggish reaction kinetics, leading to unsatisfactory faradaic and energy efficiencies of the overall water electrolysis system [5–8]. To address this bottleneck, a broad range of electrocatalysts have been rationally designed and developed to accelerate HER/OER performance [9–12]. In general, electrocatalysts boost HER and OER kinetics by reducing the potential-determining step energy barrier for the intermediates, where the intermediate adsorption affinity is a core descriptor dictating the catalytic kinetics of both half-reactions [13–15]. Nevertheless, the majority of reported bifunctional candidates rely

Check for updates

Academic Editor: Mohammed Es-Souni

Received: 13 October 2026
Revised: 14 November 2026
Accepted: 16 November 2026
Published: 18 November 2026

Copyright: © 2026 by the authors. Licensee MDPI, Basel, Switzerland. This article is an open access article distributed under the terms and conditions of the Creative Commons Attribution (CC BY) license.

on multi-phase or composite architectures to reconcile the divergent adsorption requirements for hydrogen- and oxygen-containing intermediates [16–19]. In contrast, single-phase materials often face intrinsic limitations in balancing the binding strengths of these disparate intermediates, which restricts their bifunctional performances for overall water splitting. Developing single-phase catalysts that can intrinsically afford optimal adsorption of both HER and OER intermediates therefore remains highly desirable.

Nickel sulfides, as a class of Earth-abundant non-noble metal chalcogenides, have attracted intensive attention for water electrolysis owing to their favorable electronic configuration and tunable surface properties [20–24]. Nickel–sulfur stoichiometry is a critical factor governing their electrocatalytic performance, and nickel sulfides exist in multiple crystalline phases, including NiS, NiS_2, Ni_3S_4, and Ni_3S_2, each presenting distinct electronic structures and intermediate adsorption behaviors [25–28]. Among these phases, Ni_3S_2 features inherent metallic characteristics derived from continuous Ni-Ni bonding within its crystal lattice, which facilitates rapid charge transfer during electrocatalytic reactions [29–31]. Nevertheless, most previously reported nickel sulfide catalysts suffer from random compositional inhomogeneity and disordered phase mixtures. Such mixed Ni_xS_y phases inevitably generate heterogeneous surface active sites, complicating the identification of intrinsic catalytic origins and hindering precise modulation of HER/OER intermediates. In this regard, controllably synthesizing phase-dependent nickel sulfide offers an appealing strategy to clarify the phase-dependent catalytic activity of nickel sulfide and unlock their application potential as bifunctional electrocatalysts for efficient water electrolysis under alkaline media.

Given that previous comparisons between Ni_3S_2 and NiS were performed on materials with disparate nanostructures or synthesis histories, there is a lack of a unified structural baseline for rigorous phase-dependent activity evaluation. Herein, we designed a crystalline phase optimization strategy to systematically analyze how the phase composition of nickel sulfides governs electrocatalytic activity and water electrolysis performance. Monodispersed, small-sized nickel sulfide hollow nanocrystals with a tunable crystalline phase (pure Ni_3S_2, a mixed Ni_xS_y phase (which consists of Ni_3S_2 and NiS), and pure NiS) were controllably prepared by tailoring the dosage of thioacetamide (TAA) via the Schlenk reaction system. Electrochemical measurements demonstrate that pure Ni_3S_2 delivers outstanding bifunctional HER and OER activities compared to the Ni_xS_y and NiS counterparts. The activity trend ($Ni_3S_2 > Ni_xS_y > NiS$) deviates from the typical performance enhancement expected for favorable heterostructure, which offers a critical supplement to the existing understanding of nickel sulfide electrocatalysts. Notably, the HER/OER performance of Ni_3S_2 outperforms most reported bifunctional catalysts. The assembled $Ni_3S_2||Ni_3S_2$ electrolyzer achieves a low cell voltage of 1.55 V at a current density of 10 mA cm^{-2}, surpassing the Ni_xS_y-based system (1.66 V). Moreover, this electrolyzer maintains robust long-term stability, with only 0.40% activity loss following 100 h continuous electrolysis, implying its promising prospects for practical alkaline water electrolysis.

2. Experimental Section

2.1. Chemicals

All the reagents involved in experiments were analytical grade and used without further purification. Nickel acetylacetonate ($Ni(acac)_2$), thioacetamide (TAA), 1-octadecene (ODE), oleic acid (OA), and potassium hydroxide (KOH) were purchased from Aladdin Chemical Reagent Co., Ltd., Shanghai, China. Ethanol and hexane were obtained from Tianjin Kemiou Chemical Reagent Co., Ltd., Tianjin, China. Carbon cloth (CC) was purchased from Suzhou Taili Material Technology Co., Ltd., Suzhou, China.

2.2. Synthesis of Ni_3S_2, Ni_xS_y, and NiS

The monodispersed Ni_3S_2 hollow nanocrystals (Ni_3S_2) were synthesized via a Schlenk system. Typically, 260 mg of $Ni(acac)_2$ and 38 mg TAA were dispersed into a mixed solution containing 4 mL of ODE and 10 mL of OA under continuous stirring. The system was heated to 140 °C at a rate of 5 °C/min and held for 1 h to remove low-boiling impurities. Subsequently, the reaction temperature was raised to 250 °C at 5 °C/min and maintained for 1 h. The collected black product was washed several times with a hexane/ethanol mixed solvent and dried at room temperature to obtain Ni_3S_2. For comparison, Ni_xS_y and NiS hollow nanocrystals were also prepared through an identical route by tuning the dosage of TAA to 75 mg and 150 mg, respectively.

2.3. Material Characterizations

X-ray diffraction (XRD) patterns were recorded on an X-ray diffractometer (Rigaku D/max-IIIB, Cu Kα, λ = 1.5406 Å, Bruker AXS, Karlsruhe, Germany) at a scan rate of 10° min^{-1} in a range from 10° to 80°. The chemical composition measurements were performed by X-ray photoelectron spectroscopy (XPS—X-ray source energy, 1486.7 eV; binding energy calibration, 284.6 eV; background pressure, 4×10^{-9} Pa, VG Scientific, East Grinstead, UK) using Al Kα radiation. Transmission electron microscopy (TEM), high-resolution TEM (HRTEM), and element mapping were obtained from JEM-3010 (JEOL, Tokyo, Japan) with a voltage of 200 kV.

2.4. Preparation of Working Electrodes and Electrochemical Measurements

The working electrodes were prepared by mixing 5 mg of catalyst (commercialized Pt/C (20%), RuO_2, Ni_3S_2, Ni_xS_y, and NiS) in the ethanol/deionized water (v/v = 1:1, total volume is 1 mL). Subsequently, 10 μL of Nafion (5 wt%) solution was added to the above mixture to form a homogeneous slurry. The obtained catalyst slurry was uniformly coated on a CC substrate with an area of 1.0 cm × 1.5 cm, and then used as working electrode for alkaline water electrolysis evaluation. It should be noted that Nafion was employed uniformly for all catalysts with fixed electrode preparation parameters in this study to eliminate fabrication-derived variations and enable a fair comparison of the intrinsic phase-dependent electrocatalytic performance of nickel sulfides. The graphite rod and Hg/HgO were used as the counter electrode and reference electrode, respectively. Before the electrochemical test, the alkaline electrolyte was 1.0 M KOH, which was saturated with N_2 by continuous purging for more than 30 min. All electrocatalysts must endure several cyclic voltammetry (CV) tests with a scan rate of 50 mV s^{-1} to obtain stabilize the current. The linear sweep voltammogram (LSV) tests for HER were collected to obtain polarization curves with a scanning rate of 5 mV s^{-1}, while the scanning rate for OER was 1 mV s^{-1}. The potential was referred to a reversible hydrogen electrode (RHE) according to E(RHE) = E(Hg/HgO) + 0.059 × pH + 0.098 V. All polarization curves were 90% iR compensation. To ensure the reliability of LSV-derived catalytic activity, the overpotentials adopted for performance evaluation are statistically obtained from at least three independently prepared and measured electrodes. The Tafel slope (b) was calculated using the equation of η = a + blog (j), where η is the overpotential and j is the current density. The electrochemical impedance spectrum (EIS) was collected at the frequency range of 0.01–100,000 Hz (10 mV amplitude). CV curves were performed with scan rates of 10~100 mV s^{-1} to assess electrochemical double-layer capacitance (C_{dl}) within a non-faradaic potential range. The C_{dl} values of the samples were estimated by plotting $\Delta J = J_a - J_c$ against the CV scan rate, where the slope was twice that of C_{dl}. The electrochemically active surface area (ECSA) of the obtained catalysts was determined using the formula of ECSA = C_{dl}/C_s, where C_s rep-

resents the specific capacitance, which is taken as 0.04 mF based on the previous literature. The electrochemical stability was assessed by chronopotentiometry measurements.

3. Results and Discussion

3.1. Synthesis and Structural Characterization

The synthetic route for the monodispersed nickel sulfide hollow nanocrystals is illustrated in Figure 1a. In this Schlenk synthesis system, nickel acetylacetonate ($Ni(acac)_2$) and TAA serve as the nickel and sulfur sources, while oleic acid (OA) acts as the surface ligand capping agent and 1-octadecene (ODE) as the high-boiling solvent. Transmission electron microscopy (TEM) images were used to characterize the microstructures of as-prepared Ni_3S_2. As displayed in Figure 1b, Ni_3S_2 presents a typical hollow nanosphere with an average size of 171.28 nm, which was determined by measuring 20 independent nanocrystals shown in Figure S1. High-resolution TEM (HRTEM) images taken from the selected region (Figure 1c,d) exhibit clear lattice fringes. The measured interplanar spacing of 2.87 Å corresponds to the (110) plane of Ni_3S_2. The elemental mapping images (Figure 1e) confirm the successful formation of a hollow structure and demonstrate the uniform distribution of Ni and S elementals across the entire region. For contrast, Ni_xS_y and NiS hollow nanocrystals were also prepared via an identical method (Figure S2). These characterizations verify the feasibility of our synthetic strategy for the controllable preparation of Ni_3S_2, Ni_xS_y, and NiS hollow nanocrystals, enabling the systematic investigation of phase-dependent electrocatalytic behavior of nickel sulfides.

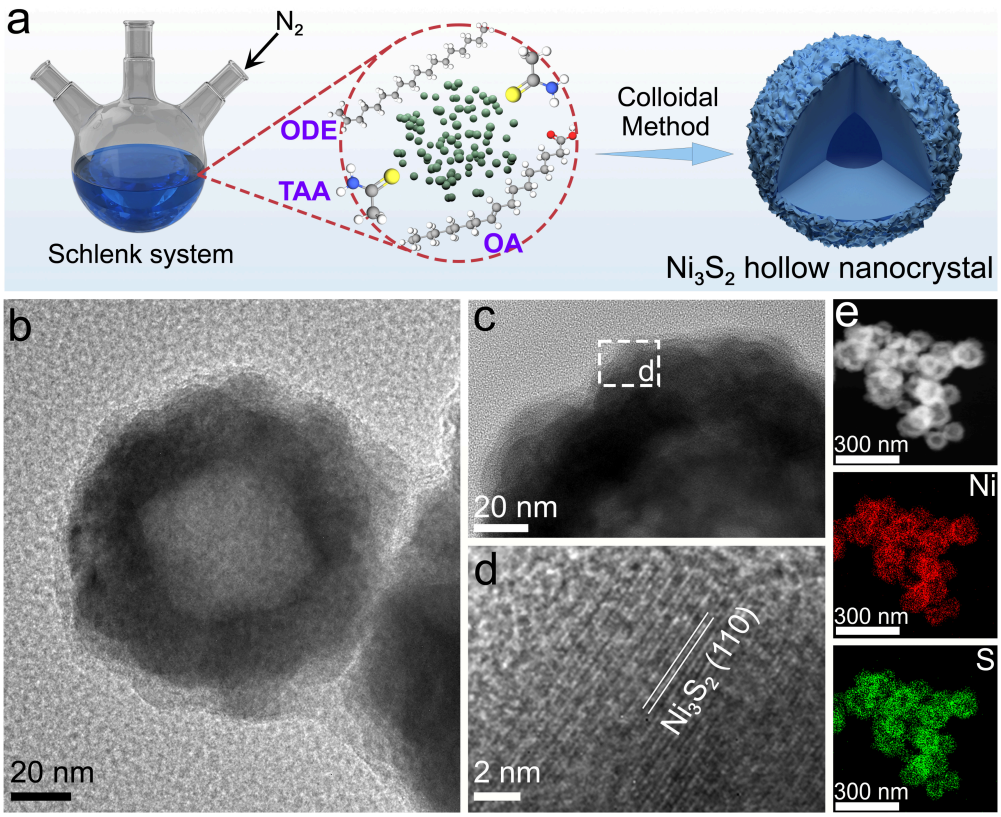


Figure 1. (**a**) Synthesis schematic diagram, (**b**,**c**) TEM images, (**d**) HRTEM image, and (**e**) element mapping of small-sized Ni_3S_2 hollow nanocrystals.

The crystal phases and structural purity of the as-prepared nickel sulfide hollow nanocrystals were investigated via X-ray diffraction (XRD). The XRD pattern of Ni_3S_2 is displayed in Figure 2a. The characteristic diffraction peaks located at 21.9°, 31.1°, 38.4°,

44.7°, 50.4°, 55.5°, 69.4°, 73.8°, and 78.0° are well indexed to the (101), (110), (021), (202), (113), (122), (131), (312), and (401) crystal planes of hexagonal Ni_3S_2 (PDF # 85-0775), confirming the successful synthesis of a high-purity Ni_3S_2 crystalline phase. For the NiS (Figure 2b), the diffraction signals observed at 30.1°, 33.8°, 34.7°, 45.9°, 53.5°, 61.7°, 62.8°, and 73.1° match well with the standard card of NiS (PDF # 75-0613), and no other diffraction peaks are detected, demonstrating the phase purity of the obtained NiS sample. Moreover, the XRD pattern in Figure 2c simultaneously exhibits the characteristic diffraction peaks of both Ni_3S_2 and NiS, meaning the obtained Ni_xS_y sample consists predominantly of Ni_3S_2 and NiS phases. Notably, no obvious shifts in the diffraction peaks are observed compared to the pure Ni_3S_2 and NiS counterparts. The above XRD results confirm that the various nickel sulfide phases have been successfully prepared.

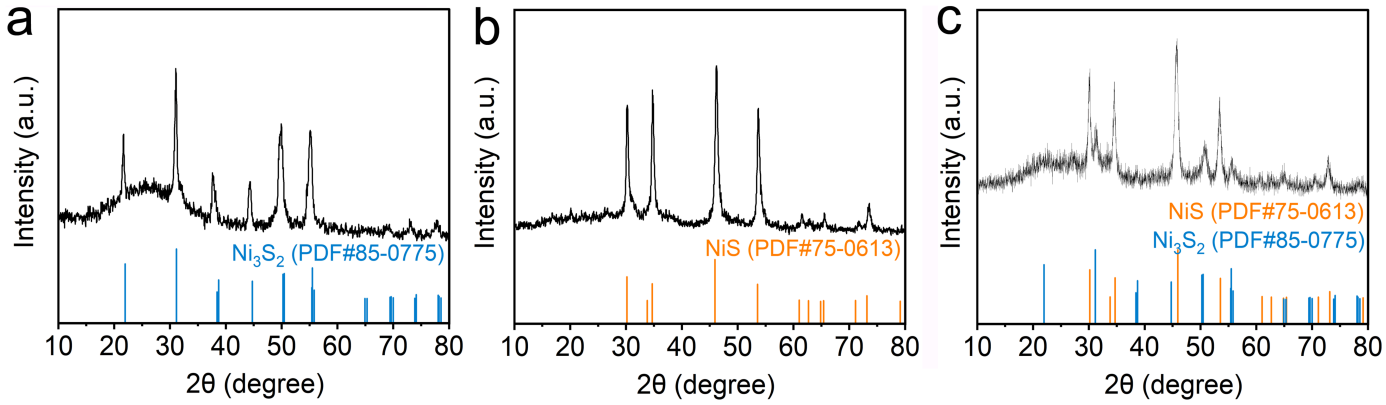


Figure 2. XRD patterns of as-synthesized (**a**) Ni_3S_2, (**b**) NiS, and (**c**) Ni_xS_y.

3.2. HER Performance

Figure 3a displays the iR-corrected linear sweep voltammogram (LSV) curves for the HER of Ni_3S_2, Ni_xS_y, NiS, and commercial Pt/C catalysts. It intuitively reveals that Ni_3S_2 delivers the best HER activity among the investigated non-noble metal catalysts. The overpotential values of various catalysts at designated current densities are summarized in Figure 3b. At the current densities of 10 and 100 mA cm^{-2}, Ni_3S_2 requires lower overpotentials (η) of 127 and 289 mV, respectively, which are markedly lower than those of the Ni_xS_y (η_{10} = 136 mV, η_{100} = 315 mV) and NiS (η_{10} = 147 mV, η_{100} = 369 mV) counterparts. Although the HER performance of Ni_3S_2 still lags behind commercial Pt/C (34 mV and 109 mV at 10 and 100 mA cm^{-2}), it compares favorably with recently reported HER electrocatalysts (Figure 3c and Table S1), indicating promising application potential. The reaction kinetics are evaluated via Tafel slopes presented in Figure 3d. Ni_3S_2 exhibits a smaller Tafel slope of 97.43 mV dec^{-1} relative to Ni_xS_y (103.64 mV dec^{-1}) and NiS (120.37 mV dec^{-1}), indicative of its accelerated HER kinetics. Furthermore, the Nyquist plots in Figure 3e demonstrate that Ni_3S_2 has the smallest interfacial charge transfer resistance (R_{ct}) of 2.42 Ω, showing a rapid interfacial charge transfer ability. The double-layer capacitance (C_{dl}) derived from non-faradaic cyclic voltammetry (CV) measurements (Figure S3) was carried out to evaluate the electrochemical active surface area (ECSA) of the catalysts. The corresponding C_{dl} values fitted from these curves are listed in Figure 3f. Notably, Ni_3S_2 delivers a larger C_{dl} value of 55.96 mF cm^{-2} compared to Ni_xS_y (51.42 mF cm^{-2}) and NiS (46.47 mF cm^{-2}). The higher C_{dl} value verifies that pure-phase Ni_3S_2 possesses more exposed active sites and a larger electrochemically active surface area, thereby endowing it with greater electrocatalytic potential for HERs. Furthermore, the ECSA-normalized LSV curves in Figure S4 show that the Ni_3S_2 exhibits higher j_{ECSA} than that of Ni_xS_y and NiS at the same potential, demonstrating the superior intrinsic activity of Ni_3S_2. The above

HER measurement results collaboratively demonstrate that the HER performance follows the trend of Ni_3S_2 > Ni_xS_y > NiS, revealing the phase-dependent catalytic behavior. More importantly, this experimental trend deviates from the typical performance feature of a favorable heterostructure, which provides indirect evidence to support our assignment that the Ni_xS_y sample consists predominantly of mixed Ni_3S_2 and NiS phases. Long-term stability is another critical criterion for evaluating practical electrocatalytic applications. As illustrated in Figure 3g, the LSV curves of Ni_3S_2 remain nearly overlapped with the initial profile after 1000 CV cycles, with only a negligible overpotential increase of 2 mV. Furthermore, the chronopotentiometry measurement indicates that Ni_3S_2 maintains 76.45% of its initial potential after 100 h of continuous operation (Figure 3h), showing relatively good durability. The post-HER TEM (Figure S5) results show that the hollow nanocrystal is largely preserved after long-term HER operation.

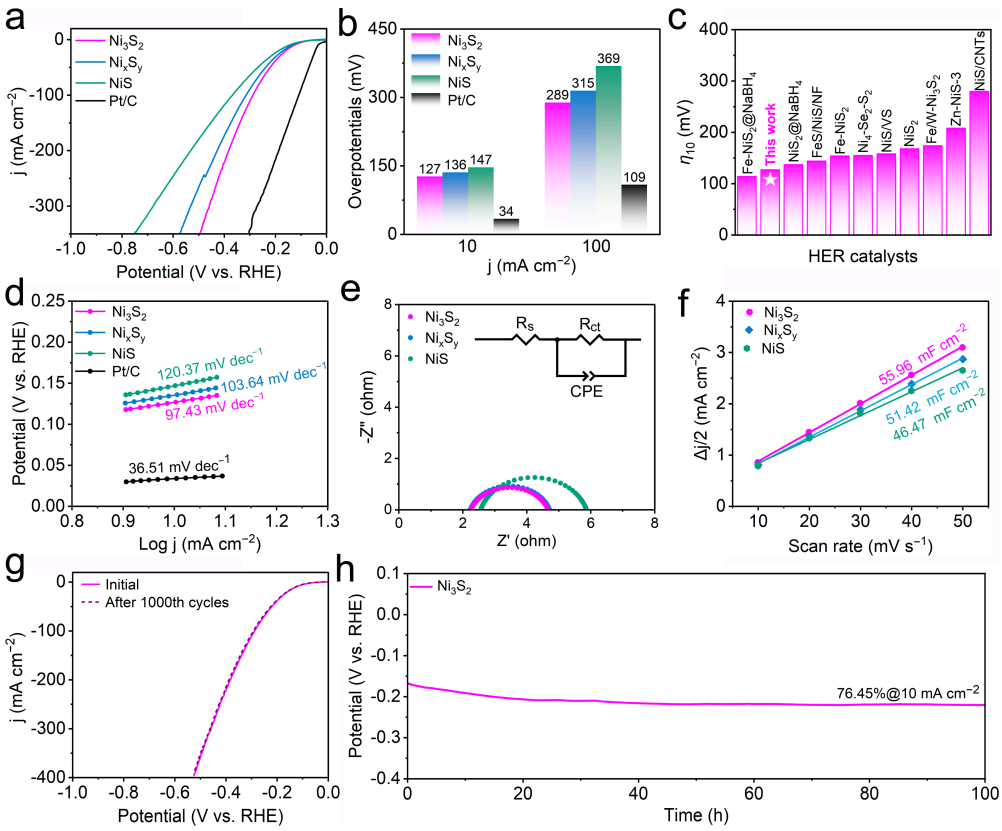


Figure 3. (**a**) HER LSV curves and (**b**) overpotential comparisons at 10 and 100 mA cm^{-2} for Ni_3S_2, Ni_xS_y, and NiS. (**c**) Comparison of η_{10} of Ni_3S_2 with reported HER catalysts. (**d**) Tafel plots, (**e**) Nyquist plots, and (**f**) C_{dl} of Ni_3S_2, Ni_xS_y, and NiS. (**g**) LSV curves before and after 1000 cycles and (**h**) chronopotentiometry curves of Ni_3S_2.

3.3. OER Performance

The OER performance of the as-synthesized catalysts were systematically evaluated under identical alkaline conditions. The LSV curves in Figure 4a demonstrate that pure-phase Ni_3S_2 exhibits the optimal OER activity among all tested samples. The overpotentials required at current densities of 10 and 100 mA cm^{-2} are summarized in Figure 4b. Specifically, Ni_3S_2 shows low overpotentials of 223 and 398 mV, which are substantially lower than those of Ni_xS_y (η_{10} = 305 mV, η_{100} = 468 mV), NiS (η_{10} = 349 mV, η_{100} = 638 mV), and commercial RuO_2 (η_{10} = 268 mV, η_{100} = 535 mV). Such superior OER performance surpasses most previously reported electrocatalysts (Figure 4c and Table S2), further implying its competitive advantages toward alkaline OER catalysis. Tafel slope analysis was further

conducted to elucidate the OER kinetics (Figure 4d). Ni_3S_2 possesses the smallest Tafel slope of 79.35 mV dec^{-1} compared to Ni_xS_y (96.52 mV dec^{-1}), NiS (156.85 mV dec^{-1}), and RuO_2 (92.54 mV dec^{-1}), confirming its significantly faster OER kinetic process. In addition, the Nyquist plots reveal that Ni_3S_2 exhibits the minimum R_{ct} among these as-prepared catalysts (Figure 4e), verifying its favorable interfacial electron transfer capability and superior catalytic potential. The ECSA of these catalysts were estimated by calculating the C_{dl} from non-faradaic CV tests at various scan rates (Figure S6). The corresponding C_{dl} values are displayed in Figure 4f. Ni_3S_2 achieves a higher C_{dl} value of 5.15 mF cm^{-2} than Ni_xS_y (3.33 mF cm^{-2}) and NiS (3.04 mF cm^{-2}). As shown in Figure S7, Ni_3S_2 exhibits higher j_{ECSA} than that of Ni_xS_y and NiS at the same potential, further implying its superior intrinsic activity for OER. The enlarged ECSA and j_{ECSA} enable Ni_3S_2 to expose abundant accessible surface active sites, thereby fundamentally boosting its intrinsic OER electrocatalytic activity. Consistent with the HER results, the OER performance also follows a distinct phase-dependent trend of Ni_3S_2 > Ni_xS_y > NiS, confirming that the pure Ni_3S_2 phase is the most favorable crystalline structure for bifunctional water electrolysis among nickel sulfide polymorphs. Meanwhile, this activity trend contradicts the characteristic behavior of a favorable heterostructure, indirectly supporting that Ni_xS_y is primarily a mixture of Ni_3S_2 and NiS.

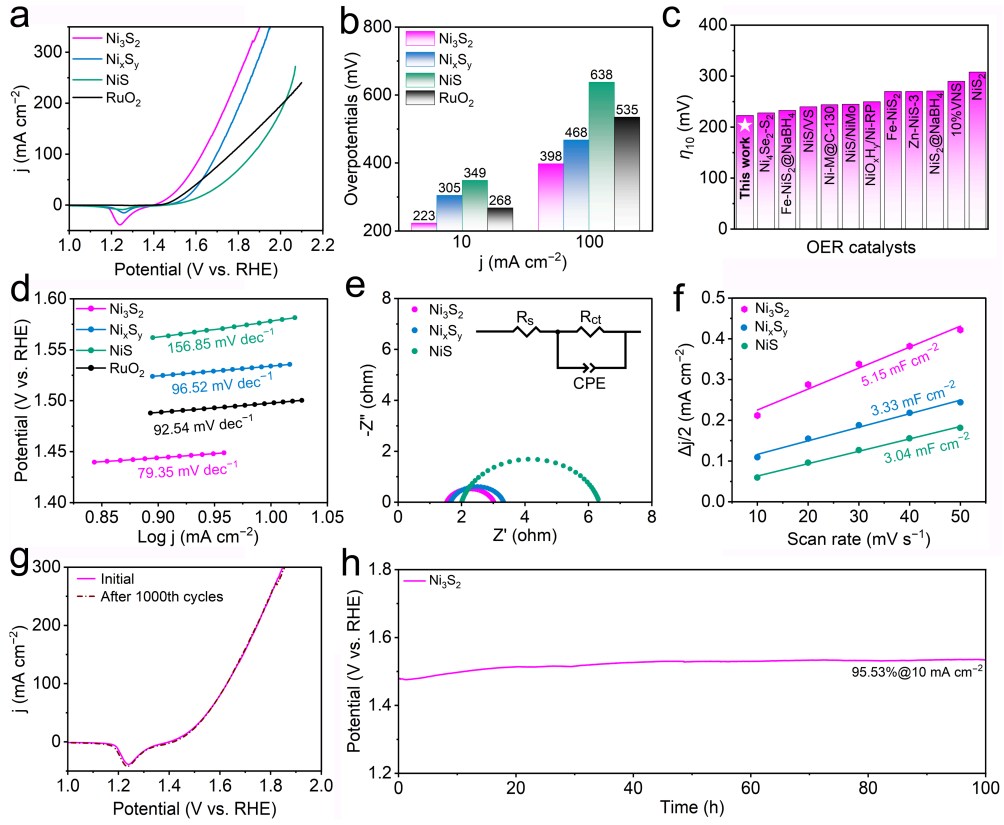


Figure 4. (**a**) OER LSV curves and (**b**) overpotential comparisons at 10 and 100 mA cm^{-2} for Ni_3S_2, Ni_xS_y, and NiS. (**c**) Comparison of η_{10} of Ni_3S_2 with reported OER catalysts. (**d**) Tafel plots, (**e**) Nyquist plots, and (**f**) C_{dl} of Ni_3S_2, Ni_xS_y, and NiS. (**g**) LSV curves before and after 1000 cycles and (**h**) chronopotentiometry curves of Ni_3S_2.

The OER stability of Ni_3S_2 was evaluated via 1000-cycle CV cycling and chronopotentiometry measurements. As shown in Figure 4g, only a 9 mV increase in overpotential is observed for the LSV curve after 1000 CV cycles. Moreover, Ni_3S_2 retains 95.53% of its initial activity after 100 h of continuous testing in alkaline electrolytes (Figure 4h). The

post-OER TEM image indicates that Ni_3S_2 retains its original morphology and structural integrity (Figure S8a). The HRTEM image confirms the formation of a new NiOOH phase alongside the intrinsic Ni_3S_2 (Figure S8b), indicating the in situ generation of NiOOH. XPS measurements were conducted to probe the evolution of the surface chemical state, as presented in Figure S9. The Ni 2p spectrum displays two pairs of characteristic peaks assigned to Ni^{3+} species and satellite peaks (sat.) (Figure S9a), indicative of the surface oxidation during the OER process [32–34]. The S 2p spectrum (Figure S9b) exhibits intensified S-O signals and attenuated S 2p peaks, which originates from sulfur oxidation and possible sulfur leaching [35–37]. In the O 1s XPS spectrum (Figure S9c), the peaks assigned to the Ni-O and metal hydroxyl species (M-OH) were observed, indicating the generation of NiOOH layer [38,39]. These post-OER characterizations confirm that long-term OER operation triggers significant surface oxidation and formation of NiOOH on the surface.

3.4. Overall Water Splitting Performance

Encouraged by the excellent HER and OER activities of Ni_3S_2, a $Ni_3S_2||Ni_3S_2$ electrolyzer was assembled using Ni_3S_2 for both the cathode and anode catalysts (Figure 5a). As depicted in Figure 5b, this electrolyzer delivers a low cell voltage of 1.55 V at 10 mA cm^{-2}, which is much lower than that of the $Ni_xS_y||Ni_xS_y$ counterpart (1.66 V). It further demonstrates that the mixture lacks effective heterojunction synergistic effects and essentially behaves as a poorly performing mixed phase. The water drainage method was adopted to quantify the generated H_2 and O_2 gases. During the testing process, the electrolyzer was kept at a stable ambient temperature, and sufficient pre-electrolysis was performed to saturate the electrolyte with H_2/O_2 prior to data recording, so as to mitigate errors arising from gas dissolution. The measured volumetric H_2/O_2 ratio approaches the theoretical stoichiometric value of 2:1 (Figure 5c), and nearly 100% faradaic efficiencies are achieved for both products. Furthermore, the $Ni_3S_2||Ni_3S_2$ electrolyzer exhibits remarkable operational durability (Figure 5d), with merely a 0.40% performance decay over 100 h of continuous electrolysis, highlighting its great promise for alkaline water electrocatalysis applications.

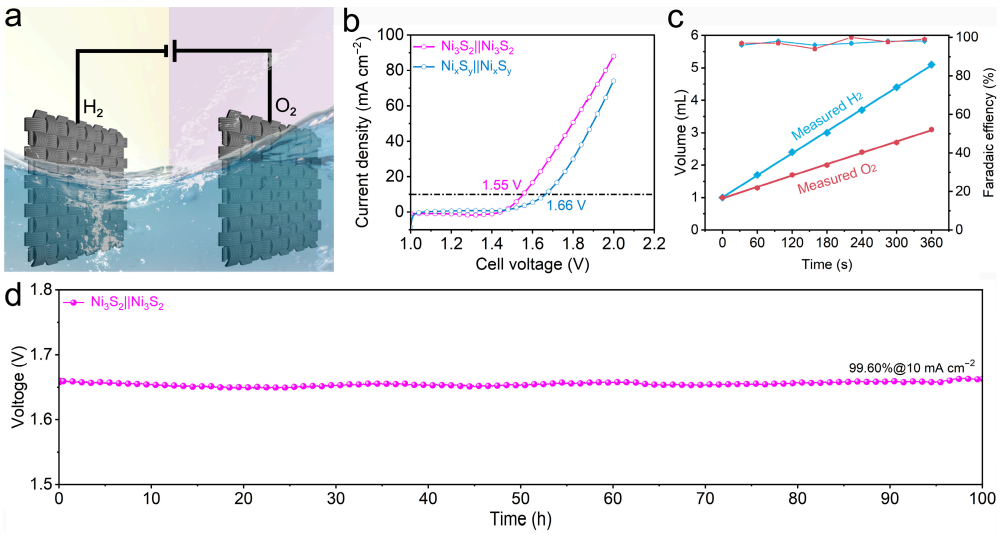


Figure 5. (**a**) Schematic illustration of OWS. (**b**) LSV curves of the $Ni_3S_2||Ni_3S_2$ and $Ni_xS_y||Ni_xS_y$ electrolyzers, where the dotted line means the cell voltage at 10 mA cm^{-2}. (**c**) Faradaic efficiency and (**d**) chronopotentiometry curve of the $Ni_3S_2||Ni_3S_2$ electrolyzer.

4. Conclusions

In summary, a series of monodispersed nickel sulfide hollow nanocrystals with tunable phase compositions, including Ni_3S_2, Ni_xS_y, and NiS, were successfully synthesized via a

facile Schlenk system by adjusting the TAA dosage. Comprehensive structural characterizations and electrochemical results have systematically revealed the intrinsic phase-dependent electrocatalytic behavior of nickel sulfide. Compared with Ni_xS_y and NiS, pure-phase Ni_3S_2 exhibited an increased electrochemical active area and accelerated charge transfer capability, thus delivering excellent bifunctional electrocatalytic activity. As a result, the assembled $Ni_3S_2||Ni_3S_2$ electrolyzer achieved a low cell voltage of 1.55 V at 10 mA cm^{-2}, with nearly 100% faradaic efficiency, remarkable long-term stability, and only a 0.40% performance decay after 100 h continuous operation. This work systematically clarifies the phase–activity correlation of nickel sulfide electrocatalysts and demonstrates that pure-phase Ni_3S_2 hollow nanocrystals are highly promising bifunctional electrocatalysts for practical alkaline water electrolysis.

Supplementary Materials: The following supporting information can be downloaded at: https://www.mdpi.com/article/10.3390/nano16221488/s1, Figure S1: TEM image of Ni_3S_2; Figure S2: TEM images of (a) Ni_xS_y and (b) NiS nanocrystals; Figure S3: HER CV curves of (a) Ni_3S_2, (b) Ni_xS_y, and (c) NiS, with different scanning rates; Figure S4: ECSA-normalized LSV curves of Ni_3S_2, Ni_xS_y, and NiS; Figure S5: TEM image of Ni_3S_2 after the alkaline HER stability test; Figure S6: OER CV curves of (a) Ni_3S_2, (b) Ni_xS_y, and (c) NiS, with different scanning rates; Figure S7: ECSA-normalized LSV curves of Ni_3S_2, Ni_xS_y, and NiS; Figure S8: (a) TEM and (b) HRTEM images of Ni_3S_2 after the alkaline OER stability test; Figure S9: Post-OER XPS spectra of (a) Ni 2p, (b) S 2p, and (c) O 1s for Ni_3S_2; Table S1: Comparison of HER performances with reported catalysts, consistent with the listed references in Figure 3c; Table S2: Comparison of OER performances with reported catalysts, consistent with the listed references in Figure 4c.

Author Contributions: Conceptualization, X.W.; Methodology, C.L., H.X., F.C., Y.W. and X.W.; Software, C.L., H.X., F.C., J.W. and L.S.; Validation, Y.W.; Formal analysis, C.L., L.S. and G.W.; Investigation, C.L., L.S. and Y.W.; Data curation, H.X., F.C. and J.W.; Writing—original draft preparation, C.L.; Writing—review and editing, X.W.; Visualization, C.L., G.W. and X.W.; Supervision, X.W.; Project administration, X.W.; Funding acquisition, X.W. All authors have read and agreed to the published version of the manuscript.

Funding: This research received no external funding.

Data Availability Statement: The original contributions presented in this study are included in the article and Supplementary Materials. Further inquiries can be directed to the corresponding author.

Conflicts of Interest: The authors declare no conflicts of interest.

References

1. Xie, H.; Zhao, Z.; Liu, T.; Wu, Y.; Lan, C.; Jiang, W.; Zhu, L.; Wang, Y.; Yang, D.; Shao, Z. A membrane-based seawater electrolyser for hydrogen generation. *Nature* **2022**, *612*, 673–678. [CrossRef]
2. Jiao, Y.-Q.; Yan, H.-J.; Tian, C.-G.; Fu, H.-G. Structure Engineering and Electronic Modulation of Transition Metal Interstitial Compounds for Electrocatalytic Water Splitting. *Acc. Mater. Res.* **2023**, *4*, 42–56. [CrossRef]
3. Xu, T.; Lu, Z.; Yu, L.; Xin, W.; Sun, J.; Zhou, H.; Jiao, Y.; Wang, X.; Lv, C. Heterointerface engineering of vanadium oxide/cobalt nitride as efficient electrocatalysts for alkaline overall water splitting. *Chem. Commun.* **2025**, *61*, 6134–6137. [CrossRef]
4. Yang, J.; Gong, S.; Liu, S.; Wu, X.; Guo, Z.; Zhao, Y.; Chen, C. A comprehensive review of high entropy oxides electrocatalysts: Advances, challenges, and prospects. *Nano Res.* **2025**, *18*, 94907774. [CrossRef]
5. An, B.; Li, X.; Li, L.; Dai, Z.; Li, N.; Gao, Y.; Ge, L. Review and perspective on the rational design and structural modulation of transition metal phosphides for efficient electrocatalytic water splitting. *Coord. Chem. Rev.* **2026**, *550*, 217406. [CrossRef]
6. Wang, X.; Sha, N.; Zhao, N.; Su, T.; Lv, C.; Yang, L.; Xie, Y.; Ye, K. Structure engineering and surface reconstruction enabling $MoNi_4$ hollow nanocube for efficient urea-assisted water electrolysis. *Chem. Eng. J.* **2024**, *499*, 156119. [CrossRef]
7. Yu, L.; Liu, C.; Sun, L.; Kan, W.; Xie, Y.; Wang, X.; Cao, Y.; Zhao, B.; Lv, C. Boosting hydrogen evolution and triiodide reduction via electronic coupling on a (1T, 2H) MoS_2@N-doped carbon dodecahedron. *Inorg. Chem. Front.* **2025**, *12*, 4844–4855. [CrossRef]
8. Lv, C.; Zhou, H.; Chen, F.; Zhang, Y.; Wang, X.; Jiao, Y. Electronic modulation of Ni_2P by cobalt doping enables high-efficiency and chloride-resistant alkaline seawater electrolysis. *Chem. Commun.* **2026**, *62*, 17409–17412. [CrossRef]

9. Fan, Y.; Li, Z.; Liu, Y.; Liu, J.; Wang, D.; Yan, H.; Gubanov, A.I.; Wu, A.; Tian, C. Nickel-Based Hollow Spheres with Optimized Interfacial Electronic Structures by Highly Dispersed MoN for Efficient Urea Electrolysis. *Adv. Funct. Mater.* **2025**, *35*, 2421222. [CrossRef]
10. Luo, B.; Wu, Y.; Chen, T.; Marini, C.; Villalobos-Portillo, E.; Dong, L.; Li, D.; Li, B.; He, H.; Chen, Z. Tailoring atomic-level electron redistribution of metal phosphides/oxides heterostructural catalyst for efficient alkaline freshwater/seawater hydrogen evolution. *J. Mater. Sci. Technol.* **2027**, *278*, 114–122. [CrossRef]
11. Lv, C.; Yu, L.; Wang, X.; Yin, J.; Zhu, K.; Xie, Y.; Zhu, J.; Ye, K. Modulating hydrogen/oxygen intermediates adsorption via dual built-in electric fields-driven electron transfer at triphasic heterointerface for efficient seawater electrolysis. *Chem. Eng. J.* **2026**, *535*, 175340. [CrossRef]
12. Yang, S.; Wang, G.; Yang, W.; Li, X.; Lv, C.; Wu, A.; Yan, H.; Jiao, Y. Low-Loading Pt Nanoparticles Anchored on Niobium Nitride for Highly Efficient Alkaline Hydrogen Evolution. *Nanomaterials* **2026**, *16*, 751. [CrossRef]
13. Ren, X.; Qiu, L.; Li, M.; Tian, F.; He, L.; Guo, X.; Wu, F.; Liu, Y.; Sheng, J.; Yang, W.; et al. Hierarchically interfacial sulfide/phosphides achieve industry-level water electrolyzer in alkaline conditions at 3 A cm^{-2}. *Appl. Catal. B Environ. Energy* **2025**, *378*, 125622. [CrossRef]
14. Liu, Y.; Li, L.; Li, X.; Xu, Y.; Wu, D.; Sakthivel, T.; Guo, Z.; Zhao, X.; Dai, Z. Asymmetric tacticity navigates the localized metal spin state for sustainable alkaline/sea water oxidation. *Sci. Adv.* **2025**, *11*, eads0861. [CrossRef]
15. Wang, W.; Bai, F.; Chu, K.; Cai, M.; Xu, X.; Guo, Z.; Zhang, X.; Qin, J.; Huang, Y.; Song, J.-L. Proton Flux Engineering via Built-in Electric Fields in N-doped CuO@Co_3O_4@$Ni(OH)_2$ Heterostructure for Rechargeable Zn-NO_3^-/5-Hydroxymethylfurfural Multielectron Transfer Systems. *Angew. Chem. Int. Ed.* **2025**, *64*, e202514438. [CrossRef]
16. Qiao, L.; Zhu, A.; Liu, D.; Feng, J.; Chen, Y.; Chen, M.; Zhou, P.; Yin, L.; Wu, R.; Ng, K.W.; et al. Crystalline phosphides/amorphous oxides composite for energy-saving hydrogen production assisted by efficient urea oxidation reaction. *Chem. Eng. J.* **2023**, *454*, 140380. [CrossRef]
17. Shi, Z.; Zhang, X.; Lin, X.; Liu, G.; Ling, C.; Xi, S.; Chen, B.; Ge, Y.; Tan, C.; Lai, Z.; et al. Phase-dependent growth of Pt on MoS_2 for highly efficient H_2 evolution. *Nature* **2023**, *621*, 300–305. [CrossRef]
18. Zhou, H.; Feng, Y.; Huo, S.; Sun, L.; Jiao, Y.; Lv, C.; Wang, X. Mo-Doped Ni_2P/FeP_4 Heterostructure with Enhanced Interfacial Charge Transfer and Electron Availability for Efficient Water Electrolysis at Large Current Densities. *ACS Sustain. Chem. Eng.* **2026**, *14*, 12180–12189. [CrossRef]
19. Ni, C.; Gao, X.; Yang, H.; Dong, J.; Wang, J.; He, C.; Li, Z.; Xu, H.; Tian, L. Dual-phase engineered hierarchical CoP enables dynamic reconstruction and multimetallic synergy for superior oxygen evolution. *Fuel* **2026**, *405*, 136533. [CrossRef]
20. Ding, X.; Liu, D.; Zhao, P.; Chen, X.; Wang, H.; Oropeza, F.E.; Gorni, G.; Barawi, M.; García-Tecedor, M.; de la Peña O'Shea, V.A.; et al. Dynamic restructuring of nickel sulfides for electrocatalytic hydrogen evolution reaction. *Nat. Commun.* **2024**, *15*, 5336. [CrossRef]
21. Sun, Y.-l.; Sun, Y.-y.; Zhang, Y.; Yanagida, T.; Ho, J.C.; Yip, S. Iron-Cobalt Co-Doped Nickel Sulfides: A Robust Electrocatalyst for High-Current-Density Seawater Splitting. *Adv. Funct. Mater.* **2026**, *36*, e17978. [CrossRef]
22. Xu, W.; Zhao, R.; Li, Q.; Sun, B.; Wu, J.; Zhong, W.; Gao, Y.; Nan, X.; Huang, Q.; Yang, Y.; et al. Overall Water Splitting on The NiS/NiS_2 Heterostructures Featuring Self-Equilibrium Orbital Occupancy. *Adv. Energy Mater.* **2023**, *13*, 2300978. [CrossRef]
23. Ouyang, D.; Liu, H.; Zhou, Q.; Feng, C. Heterostructure MoS_2/NiS supported on 3D nano-porous Ni as a highly efficient electrocatalyst for overall water splitting. *New J. Chem.* **2025**, *49*, 3119–3127. [CrossRef]
24. Zhu, X.; Ji, Z.; Wan, W.; Zhu, Y.; Lang, X.; Jiang, Q. Vacancy-rich heterogeneous $MnCo_2O_{4.5}$@NiS electrocatalyst for highly efficient overall water splitting. *J. Colloid Interface Sci.* **2025**, *678*, 878–884. [CrossRef]
25. Cui, W.-G.; Ren, X.; Wang, S.; Zhang, Y.; Li, Z.; Wang, K.; Gao, F.; Shen, Z.; Liu, Y.; Wang, X.; et al. Modulating the Structure of Interfacial Water via Oxygen-Coordinated Tungsten Single-Atom on Nickel Sulfide Slab to Boost Alkaline Hydrogen Evolution. *Adv. Energy Mater.* **2025**, *15*, e03257. [CrossRef]
26. Sun, J.; Zhao, N.; Xin, J.; Yu, M.; Lv, C.; Jiao, Y.; Wang, X. Orbital hybridization and adsorption modulating in Mo/P co-doped Ni_3S_2 enables superior urea-assisted water electrolysis at industrial current density. *Appl. Catal. B Environ. Energy* **2026**, *386*, 126446. [CrossRef]
27. Liu, Y.; Guo, J.; Liu, X.; Liu, Z.; Li, T.; Wang, S.; Zhang, C.; Wang, K.; Xu, T.; Kong, W.; et al. Corrosion-Driven Ni_3S_4 Gradient in NiFe-LDH Enables Durable Industrial-Scale Water Electrolysis. *Angew. Chem. Int. Ed.* **2025**, *64*, e202516894. [CrossRef]
28. Jiang, W.; Zhuo, X.; Yu, T.; Lu, J.; Zhai, Z.; Wen, H.; Yin, S. Regulating Reaction Intermediate Adsorption of $Co_{0.5}NiS_2$-Ni_3S_2 Nanorods for Efficient Urea Electrolysis. *ACS Sustain. Chem. Eng.* **2024**, *12*, 998–1006. [CrossRef]
29. Zhang, X.; Xia, X.; Gao, Y.; Yu, X.; Pang, Z.; Li, G.; Xu, Q.; Hsu, H.-Y.; Zhao, Y.; Hu, S.; et al. High-entropy doping strengthens Ni-S covalent bonds for industrially stable oxygen evolution. *J. Mater. Sci. Technol.* **2026**, *263*, 67–75. [CrossRef]
30. Shi, F.; Qin, J.; Wu, J.; Liu, N.; Xiao, L.; Zhou, Z.; Li, Y.; Cheng, C.; Wang, H.; Mao, J.; et al. Metal Spin-State and Low-Crystallinity Integration Enables High-Current-Density Hydrogen Evolution on Ni_3S_2 in Alkaline Water and Seawater. *Adv. Funct. Mater.* **2026**, *36*, e75755. [CrossRef]

31. Sharma, P.J.; Joshi, K.K.; Siraj, S.; Sahatiya, P.; Sumesh, C.K.; Pataniya, P.M. Vanadium-Doped Ni_3S_2: Morphological Evolution for Enhanced Industrial-Scale Water and Urea Electrolysis. *ChemSusChem* **2025**, *18*, e202401371. [CrossRef]
32. Lee, H.; Ding, G.; Wang, L.; Ding, Y.; Tang, T.; Sun, L. Suppressing Mo-Species Leaching in MoO_x/A-Ni_3S_2 Cathode for Stable Anion Exchange Membrane Water Electrolysis at Industrial-Scale Current Density. *Adv. Sci.* **2025**, *12*, 2502478. [CrossRef]
33. Wang, X.; Yu, L.; Lu, Z.; Liu, C.; Zhao, B.; Lv, C.; Xie, Y.; Kan, W. A "Two-Pronged" Strategy via Tungsten Doping and Heterostructure to Boost Hydrogen Evolution Reaction in pH-Universal Media. *ACS Sustain. Chem. Eng.* **2025**, *13*, 5633–5644. [CrossRef]
34. Mai, M.; Hoa, V.H.; Prabhakaran, S.; Dao, H.T.; Kim, D.H. Modulated electronic structure of atomic W-doped NiO/Cr_2S_3 nanotube heterostructure on nickel foam for enhanced overall water splitting. *Appl. Catal. B Environ. Energy* **2025**, *361*, 124641. [CrossRef]
35. Wang, X.; Lu, Z.; Cao, Y.; Su, T.; Yu, L.; Sun, J.; Zhao, B.; Lv, C.; Xie, Y. Multi-synergy enabling Ni-doped MoS_2@N-doped carbon composite as versatile catalysts toward hydrogen production and photovoltaics. *Carbon* **2025**, *231*, 119724. [CrossRef]
36. Yan, Q.; Liu, Y.; Zhao, Y.; Zhou, X.; Yuan, W. Molten salt-mediated electrosynthesis of MoS_2 nanosheet-supported Rh nanoclusters for highly efficient electrocatalytic hydrogen evolution. *Chem. Commun.* **2025**, *61*, 3700–3703. [CrossRef]
37. Li, N.-P.; Zhang, L.; Zhang, H.; Min, F.-F.; Wang, L.; Toan, S.; Liu, X.-J.; Hu, G.-Z. Synergistic effect between Er-doped MoS_2 nanosheets and interfacial Mo-N coupling phases for enhanced electrocatalytic hydrogen evolution. *Rare Met.* **2024**, *43*, 1301–1308. [CrossRef]
38. Bai, Z.; Chen, H.; Sha, W.; Lin, J.; Miao, J.; Xie, A.; Pan, J.; Pang, R.; Yan, K.; Wan, P.; et al. W-induced reconstruction of NiFe (oxy)hydroxides with abundant O-vacancies as efficient electrocatalysts for water oxidation. *Fuel* **2026**, *406*, 136945. [CrossRef]
39. Li, X.; Dong, Y.; Dai, Z.; Zhang, L.; An, B.; Li, N.; Gao, Y.; Ge, L. Electronic modulation of CoFeP@NiFe LDH hierarchical nanosheets for industrial water electrolysis at an ultra-low voltage of 1.67 V. *J. Colloid Interface Sci.* **2026**, *706*, 139632. [CrossRef]

Disclaimer/Publisher's Note: The statements, opinions and data contained in all publications are solely those of the individual author(s) and contributor(s) and not of MDPI and/or the editor(s). MDPI and/or the editor(s) disclaim responsibility for any injury to people or property resulting from any ideas, methods, instructions or products referred to in the content.